Carbon vacancy associates enhance the visible-light-induced photocatalytic performance of C_3N_4 nanosheets toward NO and NO_2 oxidation

Yuhan Li[a, b], Wingkei Ho[a, *], Kangle Lv[b, *], Bicheng Zhu[c], Shun Cheng Lee[d]

[a] Department of Science and Environmental Studies, The Education University of Hong Kong, Tai Po, N.T., Hong Kong, PR China

[b] Key Laboratory of Catalysis and Materials Science of the State Ethnic Affairs Commission and Ministry of Education, Hubei Province, College of Resources and Environmental Science, South-Central University for Nationalities, Wuhan 430074, PR China

[c] State Key Laboratory of Advanced Technology for Materials Synthesis and Processing, Wuhan University of Technology, Wuhan, China

[d] Department of Civil and Environmental Engineering, The Hong Kong Polytechnic University, Hung Hom, Hong Kong

1. Introduction

The extensive utilization of fossil fuels remarkably contributes to environmental contamination; as a consequence, air quality deteriorates and atmospheric pollution problems, such as greenhouse effect, ozone layer depletion, and acid rain, ensue [1]. As such, efforts have been devoted to developing sustainable and efficient air purification. Semiconductor photocatalysis has been considered as a promising strategy to address this issue and has thus achieved encouraging progress over the recent years [2–4]. Among semiconductor photocatalysts [5–7], g-C_3N_4 is an intriguing visible light-stimulated photocatalyst because of its appropriate band position, which can satisfy thermodynamic requirements for various potential photocatalytic applications, such as hydrogen evolution [8], organic pollutant degradation [9], and air purification [10]. However, the photocatalytic performance of pure g-C_3N_4, with its low specific surface area and rapid photo-generated electron–hole pair recombination, is below its expected performance. In practical applications, high-efficiency strategies should be developed to increase the surface area of g-C_3N_4 and to improve the separation/transport of photogenerated carriers.

Vacancies are common defects in photocatalysts. These vacancies function as mediators that have provided new mechanisms to promote the separation efficiency of carriers and to engineer the electronic structure of photocatalysts. Vacancies have also shown abilities to enhance photocatalytic efficiencies. As their name implies, vacancies can be easily introduced by the exposed atoms on the surface of materials escaping from a lattice. In general, these vacancies can be further divided into two types: anionic and cationic vacancies. The following anionic vacancies are of great

importance: O-vacancies in oxide photocatalysts, such as TiO_2 [11], In_2O_3 [12], $SrTiO_3$ [13], CeO_2 [14], $BiPO_4$ [15], γ-Bi_2O_3 [16], $La(OH)_3$ [17], $NiCo_2O_4$ [18], BiOI [19], HfO_2 [20], ZnO [21], SnO_2 [22], WO_3 [23], and Fe_2O_3 [24]; S-vacancies in sulfide photocatalysts, such as CdS [25] and ZnS [26]; and N-vacancies in nitride photocatalysts, including g-C_3N_4 [27, 28]. These anionic vacancies provide an optimum platform to obtain high light-harvesting capacity, rapid photo-induced charge carrier separation/transport, and evident photocatalytic performance. Cationic vacancies have also been extensively investigated because of their excellent photocatalytic reactivity, which is comparable to or even better than that of anionic vacancies. In 2007, Grey and co-workers [29] pioneered the preparation of titanium vacancies in anatase via a sol–gel method. Since then, cationic vacancies of photocatalysts have been widely explored. Enamul et al. [30] synthesized and isolated Zn vacancies in ZnO single crystals through the absorption of ultraviolet radiation. Guan et al. [31] developed bismuth vacancies in ultrathin bismuth oxychloride nanosheets to promote the photodegradation of rhodamine B (RhB) under simulated solar irradiation. Wang et al. [32] investigated the surface bismuth vacancy of $Bi_6S_2O_{15}$ core/shell nanowires with enhanced photocatalytic decomposition of methylene blue (MB) activity. Savariraj et al. [33] also demonstrated that the knit-coir-mat-like structured CuS thin films with Cu vacancy exhibit comparable electrochemical and photovoltaic performances. In addition to the widely investigated monovacancies, Bi/Cu dual vacancies of BiCuSeO have been developed, and their electrical conductivity has been significantly increased [34]. On the basis of the strong

influence of the characteristics of vacancies, such as electronic structure, charge carrier separation/transport, and superior performance, researchers suggested that the carbon vacancy in g-C_3N_4 can also influence photocatalytic performances.

Liang et al. [35] investigated g-C_3N_4 with carbon vacancies to promote the photocatalytic hydrogen evolution. However, their study focused on the contribution of carbon vacancies to photocatalytic activity in hydrogen generation but did not apply g-C_3N_4 with carbon vacancies to the photocatalytic oxidation of NO and NO_2 under visible light illumination. Therefore, the corresponding mechanism of the photocatalytic removal of NO and NO_2 remains unclear.

In this work, g-C_3N_4 nanosheets with surface carbon vacancies were fabricated through secondary thermal etching in CO_2 gas flow. As expected, the carbon vacancy effectively enhanced the photocatalytic oxidation of NO and NO_2 but decreased the concentration of in situ-generated NO_2. Considering the contradictory results of inferior optical properties, namely, high PL intensity and weak photocurrent accompanied by an enhanced photocatalytic performance, we aimed to determine the two separation/transport pathways of photo-generated electrons and to explain the photocatalytic oxidation of NO and NO_2.

2. Experimental

2.1 g-C_3N_4 synthesis

All chemicals were of analytical grade and used without further purification. Three samples were synthesized through simple thermal pyrolysis in a muffle furnace. The first bulk of g-C_3N_4 (for simplicity: CN) was obtained by heating 10 g of white

thiourea at 550 °C for 2 h at a heating rate of 15 °C·min^{-1}. A fulvous solid product was formed and cooled. Afterward, this product was ground into powder in an agate mortar. The second g-C_3N_4 sample (for simplicity: CN-CO_2-550) was synthesized with a procedure similar to that of CN; instead of 10 g of white thiourea, 10 g of sodium bicarbonate was added to the crucible in the muffle furnace. The third g-C_3N_4 sample (for simplicity: RCN-CO_2-500) was synthesized by subjecting a certain amount of CN-CO_2-550 to re-thermal treatment at 500 °C for 2 h at a heating rate of 15 °C·min^{-1}. Furthermore, 10 g of sodium bicarbonate was placed in a crucible in the muffle furnace. In all of the synthesis procedures, the gases produced during condensation were absorbed by 0.05 M dilute alkaline solution.

2.2 Characterization

The phase structures of the samples were investigated by using an X-ray diffractometer (XRD; D/max RA, Japan). The morphological characteristics and microstructures of the samples were characterized with a scanning electron microscope (SEM; JEOL JSM-6490, Japan) and a transmission electron microscope (TEM; JEM-2010, Japan). Nitrogen adsorption–desorption isotherms were obtained in a nitrogen adsorption apparatus (ASAP 2020, USA), in which all of the samples were degassed at 150 °C prior to the measurements to investigate the surface areas and pore size distribution of the samples. The samples embedded in KBr pellets were subjected to FT-IR spectroscopy in a Nicolet Nexus spectrometer to detect the functional groups on the sample surface. The surface chemical composition was investigated and the total density of state (DOS) distribution in the valence band (VB) was probed through

X-ray photoelectron spectroscopy (XPS) with Al Kα X-ray (hv = 1486.6 eV) operated at 150 W (Thermo ESCALAB 250, USA). The shift of the binding energy attributed to relative surface charging was corrected with the C 1s level at 284.8 eV as an internal standard. The optical properties of the samples were obtained in a scan UV-Vis spectrophotometer (UV-Vis DRS; UV-2450, Shimadzu, Japan) equipped with an integrating sphere assembly; $BaSO_4$ was used as the reflectance sample. The photoluminescence spectra (PL) of the samples were obtained with a fluorescence spectrophotometer (FS-2500, Japan) with a Xe lamp with an optical filter as an excitation source to investigate the recombination and separation of photo-generated electrons and holes in the samples.

2.3 Visible light photocatalytic activity

The photocatalytic activity of the as-prepared g-C_3N_4 samples was evaluated in terms of the oxidation of NO and NO_2 at ppb levels in a continuous flow reactor at ambient temperature. The volume of the rectangular reactor composed of stainless steel and covered with quartz glass was 4.5 L (30 cm × 15 cm × 10 cm; $L \times W \times H$). An LED lamp (448 nm) was used as a simulated visible light source. Afterward, 0.2 g of the as-prepared photocatalyst was added to 30 mL of H_2O and ultrasonicated for 30 min. The resulting suspension was coated onto a dish with a diameter of 11.5 cm. The coated dish was pretreated at 70 °C to evaporate water thoroughly and then cooled to room temperature prior to photocatalytic testing. NO and NO_2 gases were acquired from a compressed gas cylinder containing 50 ppm of NO and NO_2 (N_2 balance) in accordance with traceable standards recommended by the National Institute of Stands

and Technology. The initial NO and NO_2 concentrations were diluted to approximately 600 ppb by an air stream supplied by a zero-air generator (Advanced Pollution Instrumentation, A Teledyne Technologies Company, Model 701). The gas streams were completely premixed in a gas blender, and the flow rate was controlled with a mass flow controller at 1.0 $L \cdot min^{-1}$. After adsorption–desorption equilibrium was achieved, the lamp was turned on. The NO and NO_2 concentrations were continuously measured by using a chemiluminescence NO_x analyzer (Advanced Pollution Instrumentation, A Teledyne Technologies Company, Model T200), which monitors NO, NO_2, and NO_x (NO_x represents NO + NO_2), at a sampling rate of 1.0 $L \cdot min^{-1}$. The removal ratio (η) of NO and NO_2 were calculated as $\eta\ (\%) = (1 - C/C_0) \times 100\%$, where C and C_0 are the NO/NO_2 concentrations in the outlet steam and the feeding stream, respectively.

2.4 Active species trapping

Active species trapping experiments were performed to investigate the photocatalytic mechanism. Potassium iodide (KI), potassium dichromate ($K_2Cr_2O_7$), and *tert*-butyl alcohol (TBA) were chosen as scavengers of photo-generated holes, electrons, and hydroxide radical (·OH), respectively. In detail, 0.2 g of photocatalyst containing 0.002 g of KI, 0.002 g of $K_2Cr_2O_7$, or 1 mL of TBA was dispersed in 30 mL of H_2O to obtain the different samples under the same conditions. Each sample dish was used to evaluate the photocatalytic activity of visible light.

2.5 Photoelectrochemical experiments

2.5.1 Photoelectrode preparation

The g-C_3N_4 samples were deposited on a transparent conductive FTO glass substrate through electrophoretic deposition. The working electrode was prepared via the following process. First, 10 mg of g-C_3N_4 sample was dispersed in 25 mL of a 0.2 mg·mL^{-1} I_2/acetone solution under ultrasonic treatment for 2 min. A two-electrode process was used to deposit the samples at the applied potential of 20 V for 3 min. The FTO glass substrates with a coated area of approximately 1.5 cm × 2.5 cm were used for both electrodes. The deposited electrode was dried at 200 °C for 30 min to remove I_2 residues.

2.5.2 Photoelectrochemical measurements

Photoelectrochemical measurements were performed in a standard three-electrode cell containing a saturated potassium chloride–silver chloride electrode (Ag/AgCl) as a reference electrode, a platinum foil (1.0 cm × 1.0 cm) as a counter electrode, and a g-C_3N_4 sample as a working electrode. The electrolyte was 0.1 M Na_2SO_4. Linear sweeps and transient photocurrent were determined in a CHI 660D electrochemical workstation. A 300 W Xe arc lamp coupled with an AM 1.5 G global filter (100 mW·cm^{-2}) was used as a radiation source. A UV cut-off filter and a UV-Vis cut-off filter were used to simulate visible light and IR light, respectively. AC impedance was obtained in the same configuration at a cathodic bias of 20 V versus Ag/AgCl at a frequency range of 10^6–0.1 Hz.

3. Results and discussion

3.1 Structural variation

Fig. 1. TEM images of CN (a), CN-CO_2-550 (b), and RCN-CO_2-500 (c).

The SEM and TEM results of CN, CN-CO_2-550, and RCN-CO_2-500 are shown in Figs. S1 and 1. The representative morphological characteristics of an intact CN with bulk layers are illustrated in Fig. S1a. The thick layers are aggregated and linked to one another; their surfaces are rough and nonporous. The corresponding TEM image (Fig. 1a) also reveals that CN is composed of randomly aggregated thick slabs. After CO_2 is introduced to CN, CN-CO_2-550 exhibits a diminutive layered morphology. CN-CO_2-550 also contains much smaller layers than CN does (Fig. S1c). The image of CN-CO_2-550 (Fig. 1b) reveals a porous microstructure composed of randomly aggregated and interconnected layers. This result indicates that CO_2 significantly influences the morphological evolution of the g-C_3N_4 sample. Interestingly, the morphological characteristics of RCN-CO_2-500 are different when CN-CO_2-550 was treated with CO_2 and thermally etched at 500 °C. Several thin and small layers and nanoparticles are illustrated in Fig. S1c. Thin layers and small nanoparticles are

formed because of the decomposition and exfoliation of CN-CO_2-550 after this sample is subjected to secondary heating at 500 °C. The surfaces of RCN-CO_2-500 are smooth and porous; this finding suggests that gaseous CO_2 can act as a shuttle that slips into and out of the sample and etches its surfaces during the thermal process. To obtain more information on the special morphological structure, we determined the typical curved/distorted platelet morphology (Fig. 1c). This thin structure provides RCN-CO_2-500 with a large specific surface area. The distorted structure can facilitate the formation and increase the number of pores because of the twisting and folding of g-C_3N_4 networks.

The microstructure of the three samples was further investigated through EDS elemental mapping. In Fig. S2, C and N are homogeneously distributed in the three samples. After the samples were subjected to CO_2 etching and secondary thermal heating, the thinner and smaller nanosheets can be found in RCN-CO_2-500. This finding is consistent with than shown in Figs. S1 and 1.

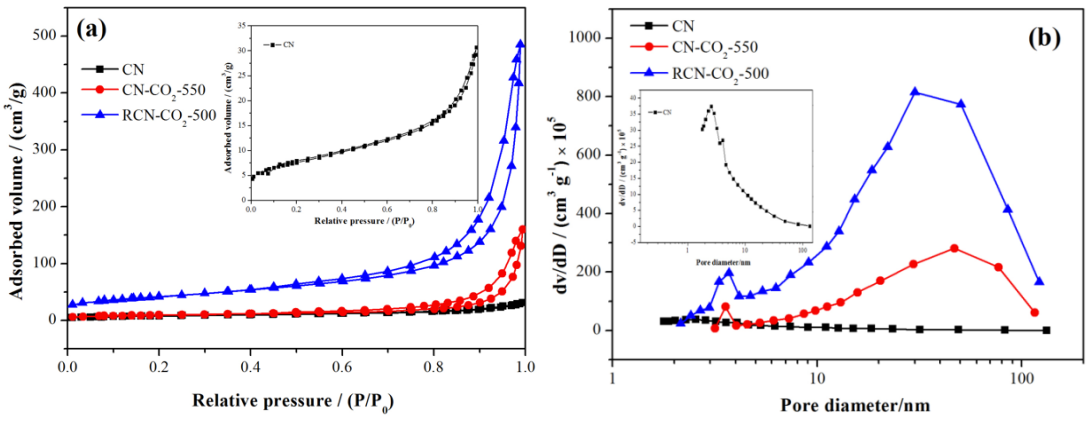

Fig. 2. N_2 adsorption–desorption isotherms (a) and the corresponding pore size distribution curves (b) of CN, CN-CO_2-550, and RCN-CO_2-500. Inset in (a) shows the enlarged view of N_2 adsorption–desorption isotherms. Inset in (b) illustrates the

corresponding pore size distribution curve of CN.

N_2 adsorption–desorption isotherms were determined and used to calculate the corresponding pore size distributions (Fig. 2) to compare the porous structures and textures of CN, CN-CO_2-550, and RCN-CO_2-500 catalysts. The corresponding structural parameters obtained from the adsorption isotherms are summarized in Table 1. In Fig. 2a, CN contains a low amount of the adsorbed N_2. CN-CO_2-550 and RCN-CO_2-500 reveal type IV isotherms with H3-type hysteresis loops in the range of 0.5–1.0 P/P_0 in accordance with the BDDT classification. This finding indicates their porosity. Moreover, the observed hysteresis loops shifted to a high relative pressure $P/P_0 \approx 1$. The results suggested the presence of large pores (>50 nm) [?]. Compared with CN-CO_2-550, RCN-CO_2-500 notably displays a visible increase in the amount of adsorbed N_2 at high relative pressures between 0.5 and 1.0. Thus, RCN-CO_2-500 yields a higher specific surface area and a larger pore volume than CN-CO_2-550 does. The pore size distribution of CN (inset in Fig. 2b) ranges from 2 nm to 10 nm. This result further indicates that the sample comprises a less porous structure formed by the random aggregation of thick layers. CN-CO_2-550 and RCN-CO_2-500 exhibit a bimodal pore size distribution with small (<5 nm) and larger pores (8–100 nm) (Fig. 2b). The small mesopores may reflect the porosity within the nanoscale sheets (Figs. 1c and 1e). The macropores presumably arise from the interstitial regions between the thin layers and the nanoparticles. Table 1 summarizes that the added CO_2 and the secondary thermal etching affect the textural structures of CN-CO_2-550 and RCN-CO_2-500. In Table 1, CN yields a small specific surface area (S_{BET}) of 27 $m^2 \cdot g^{-1}$

and a pore volume (V_{pore}) of 0.14 $cm^3 \cdot g^{-1}$; by contrast, CN-CO_2-550 obtains a high S_{BET} of 32 $m^2 \cdot g^{-1}$ and V_{pore} of 0.25 $cm^3 \cdot g^{-1}$. Among the g-C_3N_4 samples, RCN-CO_2-500 exhibits the highest S_{BET} of 147 $m^2 \cdot g^{-1}$ and V_{pore} of 0.75 $cm^3 \cdot g^{-1}$. The remarkable increase in S_{BET} of RCN-CO_2-500 can provide more reactive sites for photocatalysis to maximize the advantages of the coexistence of thin layers and nanoparticles.

Table 1. Physical properties of the as-prepared samples.

Sample	Color	$S_{BET}/m^2 \cdot g^{-1}$	$V_{pore}/cm^3 \cdot g^{-1}$	Peak pore size/nm
CN	Fulvous	27	0.14	2.4
CN-CO_2-550	Beige	32	0.25	3.7/46.8
RCN-CO_2-500	Pale	147	0.75	3.7/30.0

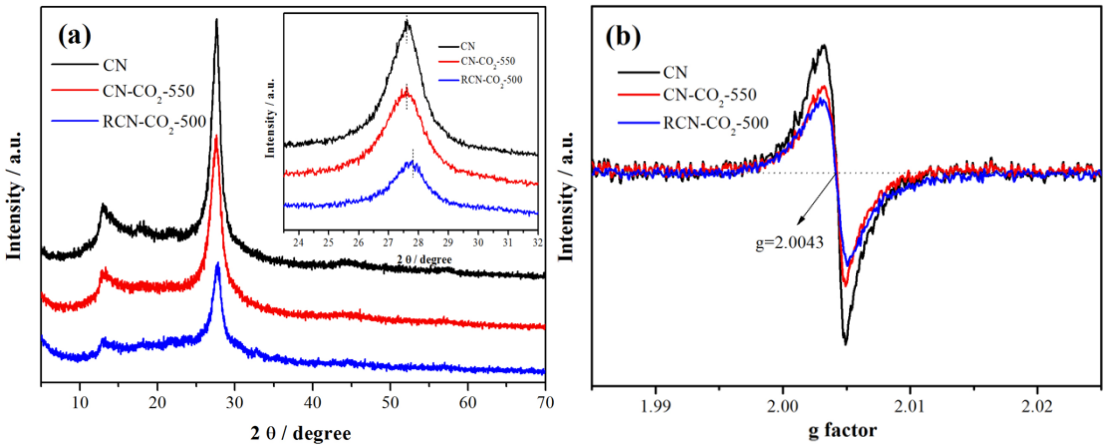

Fig. 3. XRD patterns (a) and EPR spectra (b) of CN, CN-CO_2-550, and RCN-CO_2-500 samples. Inset in (a) shows the enlarged localized profile of the (002) diffraction region.

Detailed XRD patterns were obtained to characterize the changes in the phase structure and crystallite size of the as-prepared g-C_3N_4 samples in the absence or

presence of CO_2. Fig. 3a illustrates that the diffraction peaks are coincident with those of the graphite-like hexagonal phase of g-C_3N_4 (JCPDS, Card No. 87-1526); no other diffraction peaks are detected. In the XRD patterns, the original CN displays two typical diffraction peaks, namely, the strong shoulder peak at 27.5° (d = 0.324 nm) that corresponds to the (002) interlayer diffraction of a CN graphitic-like structure and the low-angle diffraction peak at approximately 13.0° (d = 0.682 nm) that belongs to the (001) peak of the in-plane structural motif. Treated with CO_2, CN-CO_2-550 and RCN-CO_2-500 yield a greater decrease in the intensities of their diffraction peaks than the initial CN does. Therefore, crystallite size decreases, crystallization weakens, or several defects exist in their structure. These trends also indicate that CO_2 may affect the crystallization of g-C_3N_4. The enlarged localized profile of the (002) diffraction region in the samples was further investigated (inset in Fig. 3a). The peaks of CN-CO_2-550 and RCN-CO_2-500 are respectively shifted toward a higher 2θ value by approximately 0.12° and 0.31° than those of CN. Hence, the gallery distance between the basic layers of CN-CO_2-550 decreases because of the CO_2 treatment. The weak intensity of these two peaks in RCN-CO_2-500 is attributed to the depressed repulsion between the interlayers caused by defects because of CO_2 disturbance and secondary thermal etching; this finding is related to the few-layered structure and smaller planar size of RCN-CO_2-500, as observed in the SEM and TEM micrographs (Figs. S1c and 1c). The formation of defects on RCN-CO_2-500 can be confirmed through EPR spectrum analysis. In Fig. 3b, the three samples exhibit a major signal with g = 2.0043, which represents a characteristic of unpaired electrons on paramagnetic aromatic

carbon atoms. Therefore, this Lorentzian line of RCN-CO_2-500 is significantly decreased after this sample is subjected to CO_2 and secondary thermal treatment because the formation of carbon vacancies decreased the number of unpaired electrons.

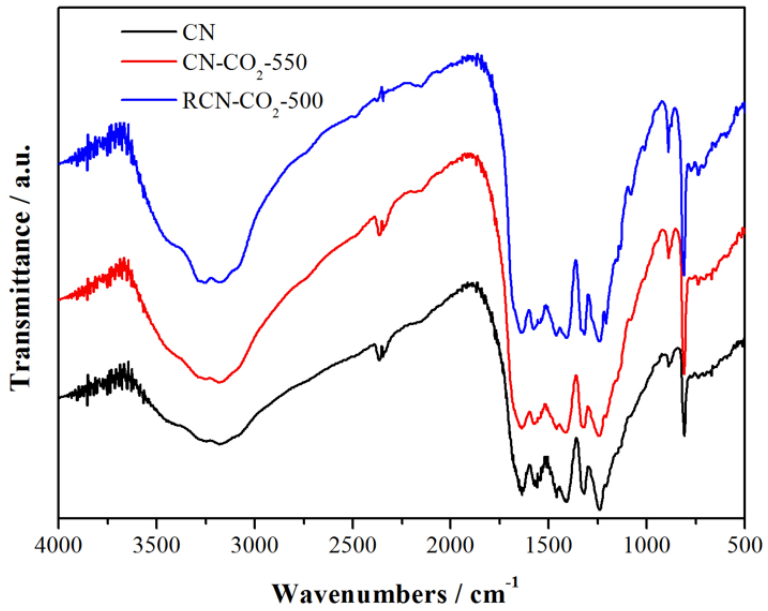

Fig. 4. FT-IR spectra of the as-prepared samples at 500–4000 cm^{-1}.

The FT-IR spectra of the three samples were obtained to investigate the influence of CO_2 and further thermal etching on the functional groups in the as-prepared samples. The featured vibration modes attributed to the representative g-C_3N_4 are shown in Fig. 4. This finding suggests that CO_2 and secondary thermal etching treatments during sample synthesis did not disrupt the basic chemical skeleton of the as-prepared samples. This result can be attributed to the high structural stability caused by the conjugated tri-s-triazine motifs in g-C_3N_4. Several strong bands in the region of 1200–1700 cm^{-1} can be assigned to the stretching vibration of the CN heterocycles; the sharp bands at approximately 808 cm^{-1} can be regarded as the

characteristic breathing mode of tri-s-triazine motifs [15]. The weak bands at 2349 cm^{-1} can be ascribed to the absorbed CO_2 molecules on the g-C_3N_4 surface. The broad bands located at 2900–3400 cm^{-1} can be attributed to the residual N–H components and the O–H bands arising from the uncondensed amino groups and the absorbed H_2O molecules, respectively. RCN-CO_2-500 shows an enhanced absorption at 2900–3400 cm^{-1}. This phenomenon indicates that the open surfaces and porous structure are enlarged. This result is consistent with the SEM and TEM micrographs.

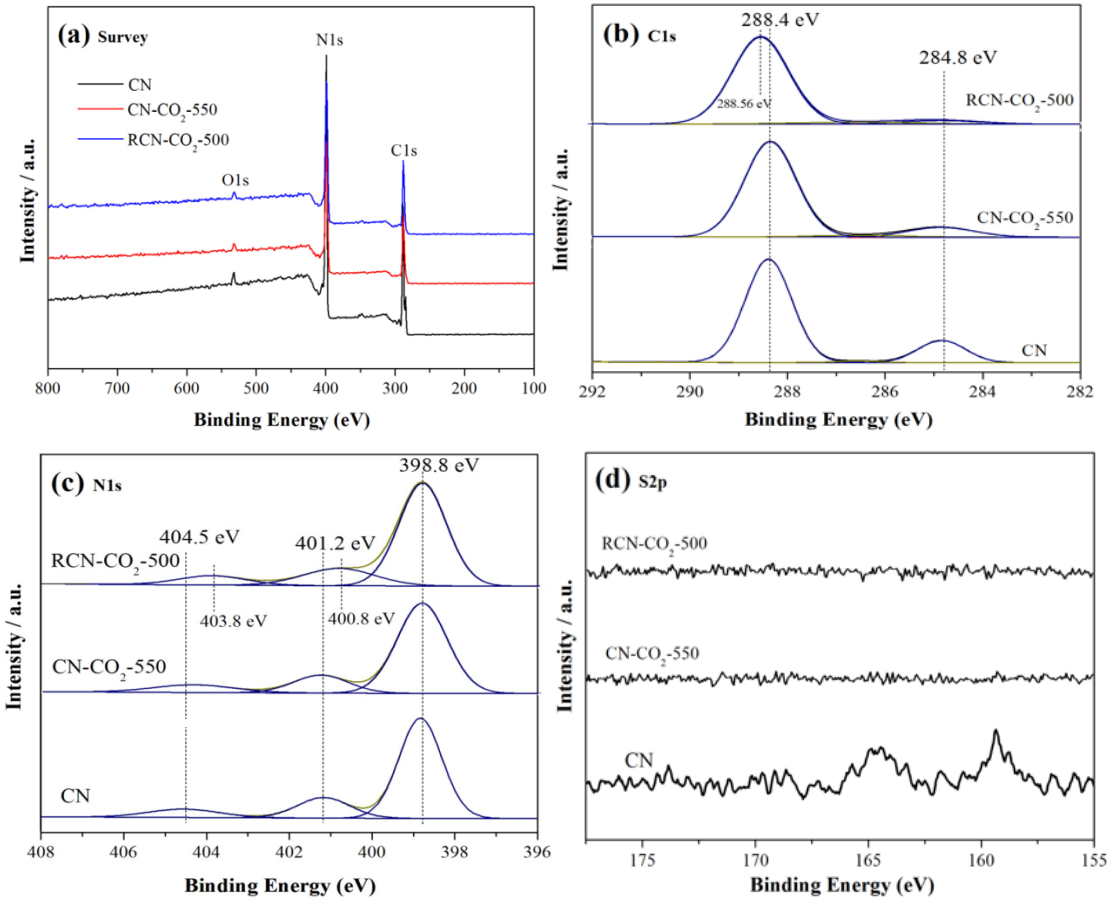

Fig. 5. High-resolution XPS spectra of (a) survey, (b) C 1s, (c) N 1s, and (d) S 2p for CN, CN-CO_2-550, and RCN-CO_2-500 samples.

The three photocatalysts were subjected to XPS to determine the specific surface

chemical states accurately. The survey scan spectra (Fig. 5a) of the as-synthesized samples reveal the typical C 1s and N 1s peaks and a weak O 1s peak. The O 1s peak may be presumably attributed to the absorbed H_2O or CO_2 molecules on the surfaces of the samples. This finding agrees with the FT-IR analysis results (Fig. 4). No peaks assigned to the sulfur species in the survey spectrum of CN can be identified because the sulfur content in the sample is very low. The detailed chemical states of the as-prepared samples are revealed in high-resolution XPS (Figs. 5b–5d).

Two main carbon species are illustrated in Fig. 5b. These carbon species correspond to the binding energies of 288.4 and 284.8 eV of the three samples. The former peak typically belongs to the sp^2-bonded carbon of the N=C–N coordination; the latter can be attributed to the sp^2-bonded carbon of C–C because of the residual carbon from the samples and the adventitious hydrocarbon from XPS instruments. In the case of RCN-CO_2-500, the C 1*s* peak at 288.4 eV of N=C–N shifts toward a higher binding energy with approximately 0.16 eV as the C/N ratio decreases (Table 2) because of the redistribution of extra electrons left by the missed carbon atoms. Therefore, the electron density around the carbon of the N=C–N coordination decreases.

The high-resolution XPS spectra of N 1*s* region (Fig. 5c) indicate that the N 1*s* region can be fitted into three peaks. The main peaks located at 398.8 eV can be ascribed to the sp^2 C–N–C. The two other peaks centered at 401.2 and 404.5 eV can be assigned to the amino functional groups with hydrogen, namely, C–N–H, attributed to the defective condensation of melon structures and the terminal nitrate groups,

charging effects, or π-excitations, respectively [9a,11]. In RCN-CO_2-500, the binding energies of N 1*s* shift significantly upward from 401.2 and 404.5 eV to 400.8 and 403.8 eV, respectively. Indeed, the electron density of nitrogen atoms in the N coordination groups increases.

The high-resolution XPS spectra of S 2*p* are shown in Fig. 5d. None of the signals in CN-CO_2-550 and RCN-CO_2-500 are attributed to S 2*p* species. Liu et al. [?] reported that the carbon atom in the CO_2 system can act as an electrophilic Lewis acid center and the oxygen atoms can function as weak nucleophilic Lewis bases. In CN-CO_2-550, the S atoms can easily escape from thiourea and thus can provide electrons to the electrophilic Lewis acid when thiourea is subjected to CO_2 treatment. Therefore, the carbon vacancies in RCN-CO_2-500 subjected to CO_2 and secondary thermal treatment are formed because of the changes in the carbon environment in thiourea. No S signals are detected in the XPS spectra of CN-CO_2-550 and RCN-CO_2-500. However, the distinct S 2*p* region can be found in CN.

Table 2. C, N, O, and S atomic rates, band gap, VB position, and CB position of CN, CN-CO_2-550, and RCN-CO_2-500 samples.

Sample	C (atm.%)	N (atm.%)	O (atm.%)	C:N	S (atm.%)	Band gap (eV)	VB position	CB position
CN	44.79	53.31	0.9	0.84	1.0	2.78	2.18	−0.60
CN-CO_2-550	44.69	53.35	1.96	0.83	0	2.85	2.13	−0.72
RCN-CO_2-500	42.39	55.19	2.42	0.77	0	3.0	2.08	−0.92

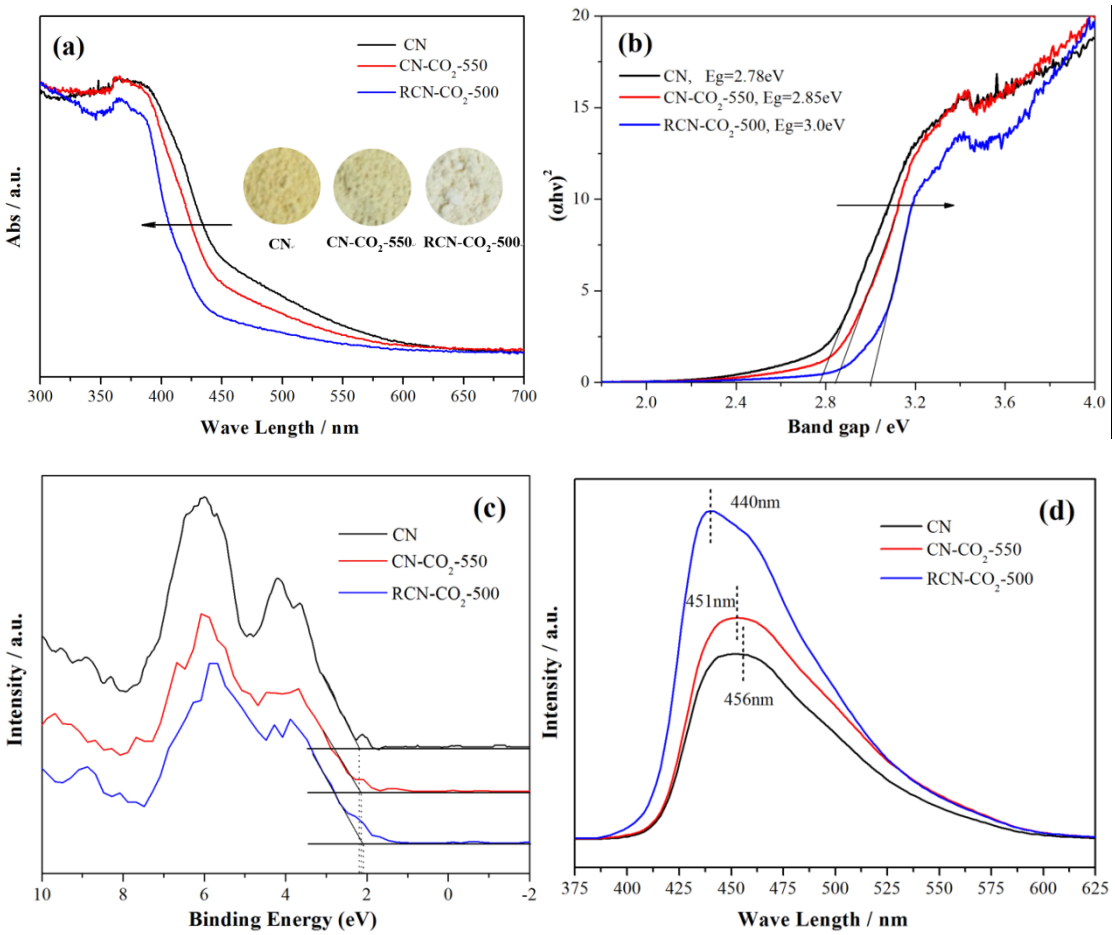

Fig. 6. UV-Vis DRS and their corresponding colors (inset) (a), plots of $(\alpha h\nu)^2$ versus photon energy (b), VB (c), and PL (d) of CN, CN-CO_2-550, and RCN-CO_2-500 samples.

CO_2 treatment and secondary thermal etching can influence the electronic and optical properties of g-C_3N_4 as a result of the different morphological characteristics and the formation of new surface states or defects within the crystal structure. UV-Vis DRS was performed because the changes in photophysical properties, namely, electronic and optical properties of the photocatalyst, can stimulate the corresponding changes in the intensity or shape of the optical spectra. In Fig. 6a, all of the samples exhibit an optical response in the UV-visible light region from 300 nm to 650 nm. In CN-CO_2-550, the absorption edge shifts toward shorter wavelengths because of the

disturbance of CO_2 during the thermal process. In RCN-CO_2-500, an evident hypochromic shift in the bandgap transition is attributed to the strong quantum confinement effects and carbon vacancy formation. In the inset of Fig. 6a, the colors of the three samples fade: from fulvous in CN to beige in CN-CO_2-550 and to pale in RCN-CO_2-500. This finding further confirmed that CO_2 treatment and thermal etching influence the photophysical properties of RCN-CO_2-500. The calculated band gap values (E_g) of the as-prepared samples based on UV-Vis DRS data are determined, as shown in Figure 6b. The band gap is increased from 2.78 eV of CN to 2.85 eV of CN-CO_2-550 and to 3.0 eV of RCN-CO_2-500. The band gap energies increase because of CO_2 treatment and secondary thermal etching. The total densities of the states of the VB XPS were obtained to investigate the energy band structure of the three samples (Fig. 6c). The VB edges of CN, CN-CO_2-550, and RCN-CO_2-500 are 2.18, 2.13, and 2.08 eV, respectively. Hence, the CB minimum energy of RCN-CO_2-500 at −0.92 eV shifts upward by 0.32 and 0.20 eV compared with those of CN and CN-CO_2-550, respectively. The detailed band gap structures of the three samples are shown in Scheme 1. The upward shifting of CB plays two crucial roles in photocatalysis. First, the photo-generated electrons become more negative because of the increase in the minimum CB to react with molecular oxygen and thus generate superoxide radicals. This phenomenon then promotes an efficient photocatalytic reaction. Second, the increased CB promotes the transfer of photo-induced electrons to surface reactants, which can hinder the photo-generated electron–hole recombination. In the RCN-CO_2-500 system, the carbon vacancies can function as a

trap for photo-generated electrons to influence the photocatalytic process. In Scheme 2, two photocatalytic pathways have been established to remove NO from RCN-CO_2-500 when carbon vacancies capture the abundant photocatalytic generated electrons: (i) the partial photoexcited electrons react with surface-adsorbed molecular oxygen to generate relevant active species for NO oxidation; (ii) the remaining photo-generated electrons may be involved in the electron–hole recombination because of their aggregation around the trapped center; as a result, inefficient migration occurs.

The PL spectra of the three samples provide additional evidence supporting the altered photophysical properties. In Figure 6d, the PL intensities of CN-CO_2-550 and RCN-CO_2-500 significantly increase; the emission blue-shifts of CN-CO_2-550 and RCN-CO_2-500 are more than 5 and 16 nm than those of CN, respectively. The PL blue-shift can be attributed to the emission of the band gap transition, with the energy of light approximately equal to the bandgap energies of the three samples. This finding is consistent with the variation of the band edges shown in Fig. 6b. The increased PL intensity indicates the formation of a weak organized g-C_3N_4 with more structural defects. These structural defects can capture the photocatalysis-generated electrons or holes to hinder the subsequent photoredox reaction; as a result, a low photocatalytic reactivity occurs. However, the increase in the CB value of RCN-CO_2-500 can enable more reductive photoexcited electrons to participate in the photocatalytic oxidation of NO; thus, an excellent photocatalytic activity takes place. The photo-generated electrons can recombine with the photo-induced holes because

photoexcited electrons are not transferred to reactants in the presence of trapped centers, namely, carbon vacancies.

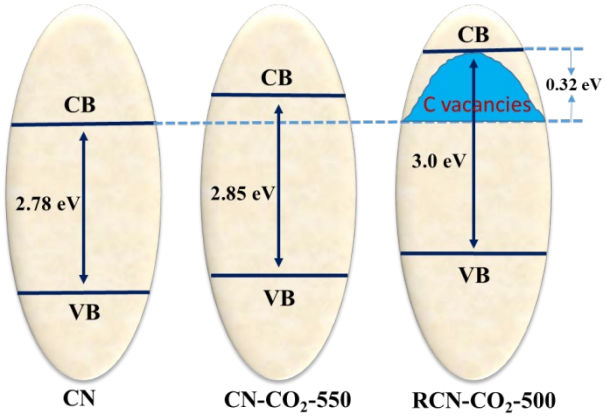

Scheme 1. Electronic band structures of CN, CN-CO_2-550, and RCN-CO_2-500.

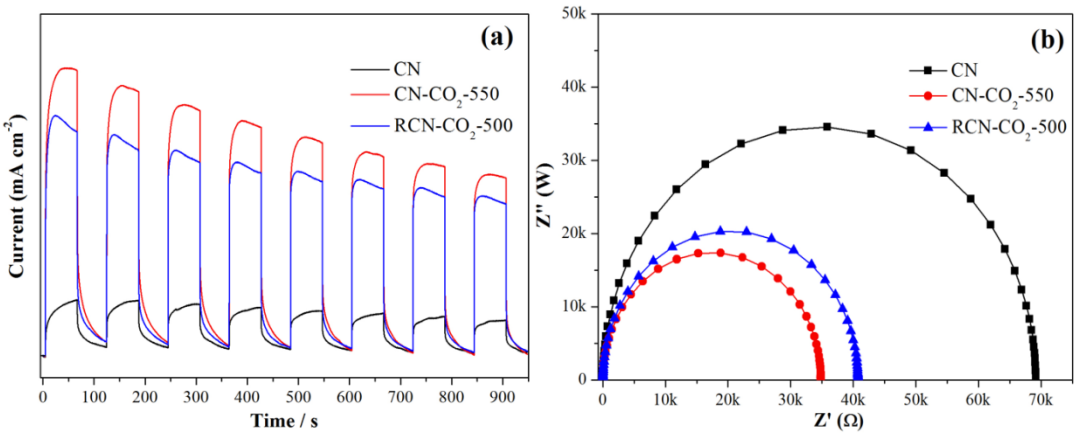

Fig. 7. Time-dependent photocurrent curves (a) and EIS Nyquist plots (b) of CN, CN-CO_2-550, and RCN-CO_2-500 electrodes under visible light irradiation (λ > 420 nm; [Na_2SO_4] = 0.1 M).

Charge separation and migration significantly influence the photocatalytic performance. A photocurrent response experiment should be implemented to reveal the effect of RCN-CO_2-500 with carbon vacancies on photocatalytic physical properties. In Fig. 7a, CN-CO_2-550 and RCN-CO_2-500 electrodes elicit faster and higher photocurrent responses than bulk CN does. This finding confirms the

advantages of CO_2 and/or secondary thermal etching treatment to promote the separation of the photo-generated carriers. However, the photocurrent intensity of RCN-CO_2-500 is weaker than that of CN-CO_2-550. Thus, the photo-generated electrons trapped by the surface carbon vacancies of RCN-CO_2-500 move along two migration paths. In one approach, the photo-generated electrons react with oxygen molecules to facilitate the photocatalytic removal of NO. In the other approach, the photo-generated electrons recombine with the photo-generated holes. Electrochemical impedance spectroscopy (EIS) was performed to investigate the electrical conductivity of the final products (Fig. 7b). The results agree with the changes in the photocurrent responses.

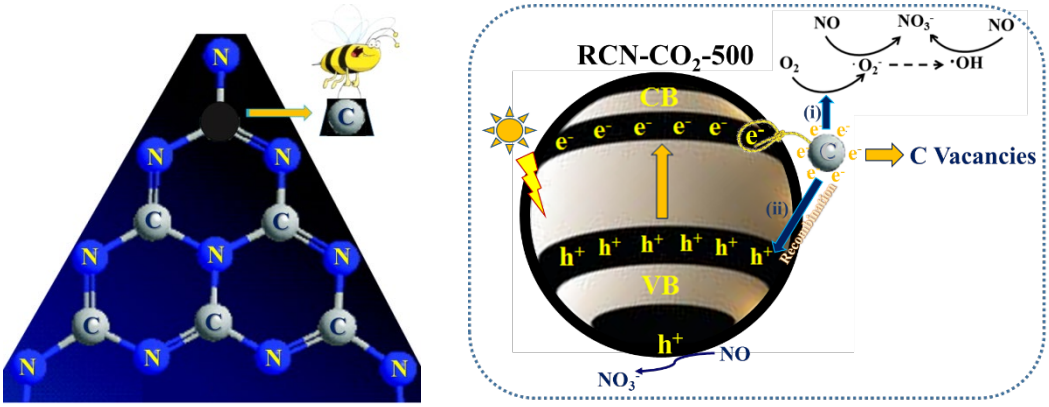

Scheme 2. Photocatalysis of RCN-CO_2-500.

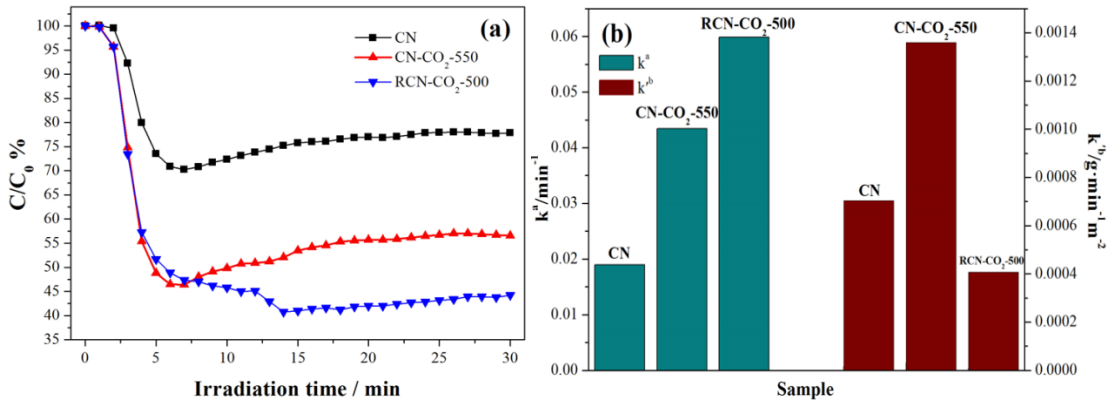

Fig. 8. Photocatalytic removal of NO in a single-pass flow of air over CN, CN-CO_2-550, and RCN-CO_2-500 samples (a) and rate constants of the photocatalytic removal of NO over CN, CN-CO_2-550, and RCN-CO_2-500 under visible light irradiation ($\lambda > 448$ nm) (b). [a]The reaction kinetics of NO removal was analyzed with a pseudo first-order model as expressed by $\ln (C_0/C) = kt$; k was normalized to the respective surface area. [b]k' refers to k normalized to the surface area (continuous reactor; NO concentration: 600 ppb).

As a common urban air pollutant in indoor environments, NO exhibits low solubility and reactivity; this pollutant also causes severe respiratory diseases, including DNA strand breaks and/or base alterations that are potentially mutagenic [?]. Therefore, this work aimed to harness environmentally friendly and economical photocatalysis technology to remove NO in air. We investigated the photocatalytic performance of the three samples by evaluating the photocatalytic removal of NO under visible light irradiation ($\lambda > 448$ nm). In Fig. 8a, the direct photolysis of NO can be neglected in the absence of either photocatalyst or light irradiation, as revealed in the results of the blank experiment. The NO degradation abilities of CN-CO_2-550 and RCN-CO_2-500 samples are higher than that of unmodified CN. This finding confirms the superiority of the CO_2-mediated synthesis of g-C_3N_4 photocatalysts. In CN and CN-CO_2-550, the NO concentration sharply decreases within 5 min; afterward, the reaction equilibrium and constant NO concentration are obtained. The removal rates of NO are 22.1% and 43.5% of CN and CN-CO_2-550, respectively. However, the NO concentration in RCN-CO_2-500 decreases much faster than the NO concentration in CN and CN-CO_2-550 after 15 min. Therefore, RCN-CO_2-500 shows the highest photocatalytic activity, with a NO degradation efficiency of 56.2% after this sample is irradiated with visible light for 30 min. The enhanced photocatalytic activity can be

attributed to abundant photo-induced active species (e.g., h^+, $\cdot O^{2-}$) and large specific surface areas. The photocatalytic removal of NO generally is consistent with the pseudo-first-order kinetic reaction:

$$\ln (C_0/C) = kt \quad (1)$$

where C is the instantaneous concentration of NO at time t (ppb), C_0 is the initial NO concentration (ppb), and k is the apparent rate constant (min^{-1}). In Fig. 8b, RCN-CO_2-500 exhibits the highest photo-degradation efficiency with an apparent rate constant of 0.06 min^{-1} (Table 3), which is 3.2 and 1.4 times higher than that of CN and CN-CO_2-550, respectively. The experimental results reveal that the photochemical properties of RCN-CO_2-500 can be modified by CO_2 and secondary thermal etching.

We normalized the photocatalytic degradation rates with the specific surface areas to rule out the effect of the specific surface areas on their photocatalytic activity and to investigate the main factors that influence the whole photocatalytic processes. In Fig. 8b and Table 3, the order of the normalized rates differed from that of the pure samples, as indicated by the comparison of the apparent rate constants of NO before and after normalization with the specific surface areas. In particular, the normalized rates of NO degradation on CN (0.70×10^{-3} $g \cdot min^{-1} \cdot m^{-2}$) and CN-$CO_2$-550 ($1.36 \times 10^{-3}$ $g \cdot min^{-1} \cdot m^{-2}$) were much faster than that of RCN-CO_2-500 (0.41×10^{-3} $g \cdot min^{-1} \cdot m^{-2}$). Therefore, the specific surface area unlikely plays a major role in the enhanced photocatalytic performance of RCN-CO_2-500 toward the photocatalytic removal of NO.

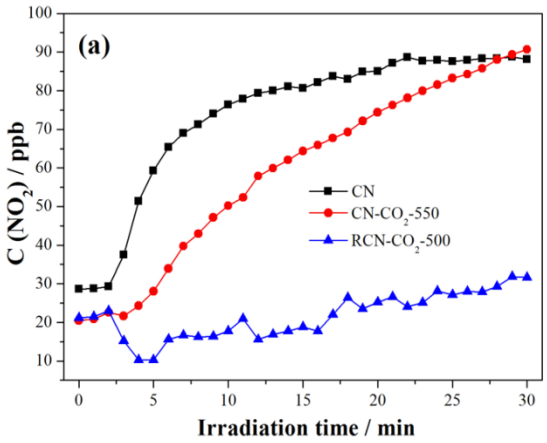

Fig. 9. Monitoring concentration of NO_2 intermediates under visible light irradiation (a) and photocatalytic removal of NO_2 in a single-pass flow of air over CN, CN-CO_2-550, and RCN-CO_2-500 samples under visible light irradiation (b) (continuous reactor; NO_2 concentration: 400 ppb).

We monitored the concentration of in-situ-generated NO_2 and found that the NO_2 concentration in the outlet gas was maintained at a relatively high level during the photoreaction on CN (88.1 ppb) and CN-CO_2-550 (90.7 ppb) but not on RCN-CO_2-500 (31.6 ppb), as shown in Fig. 9a. NO is unstable in air and can undergo spontaneous oxidation to NO_2. NO_2 can be directly toxic to the respiratory tract; its pulmonary toxicity is even thought to be several times greater than that of NO. The resulting samples were further used to remove NO_2 in air through photocatalysis (Fig. 9b).

Table 3. Removal ratios of NO and NO_2, NO_2 concentration, and reaction kinetics of NO removal of CN, CN-CO_2-550, and RCN-CO_2-500 samples.

Sample	NO removal ratio, η (%)	NO_2 concentration (ppb)	NO_2 removal ratio, η (%)	k^a (min^{-1})	k'^b ($g \cdot min^{-1} \cdot m^{-2}$)
CN	22.1	88.1		0.019	0.70×10^{-3}
CN-CO_2-550	43.5	90.7		0.043	1.36×10^{-3}
RCN-CO_2-500	56.2	31.6		0.06	0.41×10^{-3}

Possible Photocatalytic Mechanism

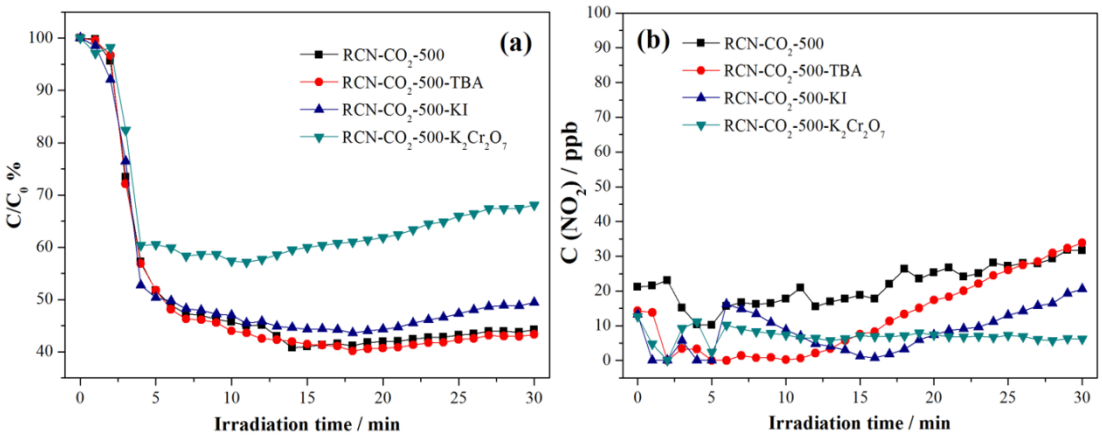

Fig. 10. Photocatalytic removal of NO over RCN-CO_2-500 in the presence of different scavengers (a) and monitoring concentration of NO_2 intermediates under visible light irradiation (b) (continuous reactor, NO concentration: 600 ppb).

The large specific surface area, strong photoabsorption capability in the available light energy region, and excellent separation efficiency of photo-generated electron–hole pairs are beneficial for the improvement of photocatalytic activities. However, our results and analyses (Fig. 8b) indicate that the normalized photocatalytic degradation rates with the specific surface areas excluded the contribution of the

increased surface area in the case of RCN-CO_2-500. The UV-Vis DRS results indicate poor photoabsorption performance; as such, this phenomenon cannot explain the significantly high photocatalytic activity.

The trapping experiments of reactive species during the RCN-CO_2-500 degradation of NO were respectively performed with KI (photo-generated holes scavengers), $K_2Cr_2O_7$ (photo-generated electrons scavengers), and TBA (·OH scavengers) to identify the main active species. In Fig. 10a, the addition of $K_2Cr_2O_7$ most acutely depressed the degradation of NO, whereas the use of KI can decrease the photocatalytic activity; the inhibition efficiencies are approximately 57% and 10%, respectively. The degradation of NO remains almost unchanged when TBA is added. Therefore, ·OH plays a minor role in the photocatalytic removal of NO in this work because ·OH is probably generated via one route: $e^- \rightarrow O_2^- \rightarrow H_2O_2 \rightarrow \cdot OH$. Therefore, that the holes and $\cdot O_2^-$ are mainly responsible for the enhanced photocatalytic activity. The variation in the monitored concentration of the in situ-generated NO_2 in the outlet gas exhibited the same trend as the change in photocatalytic activity (Figs. 10b and 10c).

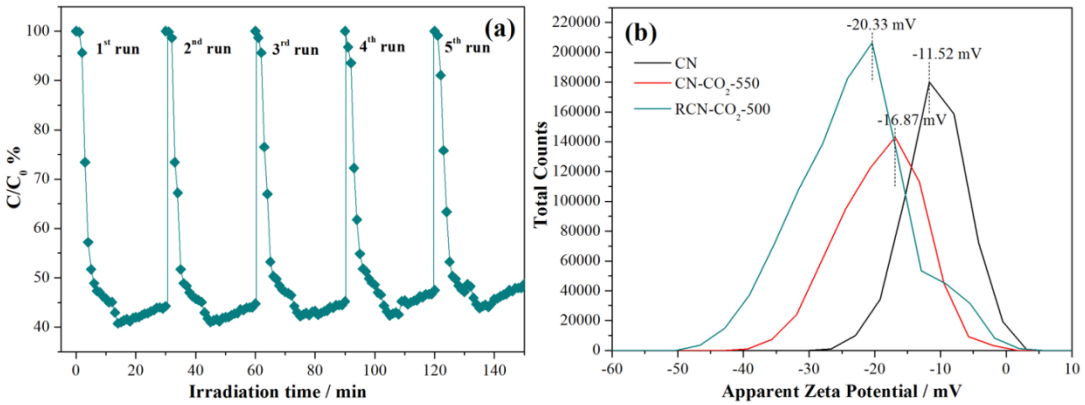

Fig. 11. Stability of RCN-CO_2-500 in five runs of photocatalytic NO degradation under visible light irradiation (a) and zeta potential values of CN, CN-CO_2-550, and RCN-CO_2-500 samples in deionized water on a zeta potential analyzer (b).

Potential photocatalysts should be cost effective, robust, durable, and stable for the photocatalytic removal of NO to be considered commercially viable. The recycling capability of RCN-CO_2-500 is evaluated with a five-run test. As illustrated in Fig. 11a, the photocatalyst did not show any evident loss of activity after five cycles were completed. In this study, RCN-CO_2-500 demonstrated satisfactory reusability in NO degradation. The zeta potential of the three samples was determined using a zeta potential analyzer by dispersing the samples into distilled water (Fig. 11b). The RCN-CO_2-500 surface yields a more negative zeta potential of approximately −20.33 mV than CN (−11.52 mV) and CN-CO_2-550 (−16.87 mV) do. This finding confirmed that RCN-CO_2-500 is stable in a liquid state.